

Article

# Local Surface Electric Field's Effect on Adsorbed Proteins' Orientation

Larbi Filali <sup>1,\*</sup>, Yamina Brahmi <sup>1</sup>, Jamal Dine Sib <sup>1</sup>, Yahya Bouizem <sup>1</sup>, Djamel Benlakehal <sup>1</sup>, Kacem Zellama <sup>2</sup>, Nathalie Lemée <sup>2</sup>, Ahmed Bouhekka <sup>1,3</sup>, Fatiha Kail <sup>1</sup>, Aissa Kebab <sup>1</sup> and Larbi Chahed <sup>1</sup>

<sup>1</sup> Laboratoire de Physique des Couches Minces et Matériaux pour l'Electronique, Université Oran 1 Ahmed Ben Bella, BP 1524, El M'naouar, 31100 Oran, Algeria; aminabra2@gmail.com (Y.B.); sibjamal@hotmail.com (J.D.S.); ybouizem@gmail.com (Y.B.); djbenlakehal@gmail.com (D.B.); bouhekkaahmed@gmail.com (A.B.); fatiha.kail@hotmail.com (F.K.); akebab2@gmail.com (A.K.); chahed.larbi@univ-oran.dz (L.C.)

<sup>2</sup> Laboratoire de Physique de la Matière Condensée, Faculté des Sciences, Université de Picardie Jules Verne, 33 rue Saint-Leu, 80039 Amiens, France; kacem.zellama@u-picardie.fr (K.Z.); nathalie.lemee@u-picardie.fr (N.L.)

<sup>3</sup> Faculty of Exact Sciences and Informatics, University Hassiba Ben Bouali of Chlef, National Road N° 19, Ouled Fares, 02000 Chlef, Algeria

\* Correspondence: larbifilali5@gmail.com

Received: 6 April 2019; Accepted: 10 May 2019; Published: 20 May 2019



**Abstract:** Hydrogenated nanocrystalline silicon, while being non-charged and non-polar, could be an ideal candidate for the non-covalent and orientation-controlled immobilization of biomolecules thanks to local electric fields around nanocrystals. To that effect, the adsorption of bovine serum albumin on substrates with different densities of nanocrystals, revealed by Raman spectroscopy and X-ray diffraction, was studied using infrared spectroscopy and atomic force microscopy. It was found that the protein–surface interactions followed different mechanisms depending on the nanostructure at the surface: hydrophobic on the non-crystalline part of the surface and electrostatic around the crystalline part. These electrostatic interactions were driven by the electric fields that arose at the junction between crystalline and amorphous structures. These electric fields were found to be strong enough to interact with the amide dipoles, thereby reorienting the adsorbed protein molecules on this part of the surface. Nevertheless, the adsorbed proteins were found to be denatured, which was due to the surface chemistry, and not affected by the nanostructure.

**Keywords:** biosensors; biomolecule orientation; protein adsorption; amide dipoles; nanocrystalline silicon; amorphous/crystalline silicon heterojunction

## 1. Introduction

The ever-growing field of nanotechnology has enabled scientists from diverse disciplines, such as physics, chemistry, engineering, molecular biology, and biotechnology, to tap into material properties at the nanoscale for the development of new technologies such as biosensors and biophotonics [1]. In particular, biosensors have a very wide range of applications, which covers their use for medical diagnosis, discovery of new drugs, food safety, defense, and many more. They are first and foremost used to detect biomolecules through the immobilization of a biological material on the biosensing device that acts as the recognition element of chemical species in a sample, producing a measurable signal [2–5]. The type of these measurable signals will determine the type of the biosensor, which can be classified as electrochemical, optical, or piezoelectrical [6]. Electrochemical biosensors, which were

the first to be scientifically proposed and successfully commercialized [7,8], are the ones targeted by this study. Their advantage is that they can sense materials without damaging the system [9].

The most important factors to consider are the specificity of the recognition and the sensitivity of the device [10]. One way of dealing with these issues is by reducing the size of the biosensor to the micro- or nano-scale which can result in a better signal-to-noise ratio, as well as the possibility of using smaller sample volumes, which means lower assay costs. Moreover, when approaching nanoscale dimensions, the surface-to-volume ratio of the sensing active area increases, while the sizes of the detecting electrode and the target analyte become comparable. This will decrease non-specific binding and the target molecule will be much more efficiently bound to the surface of the sensing device, which will allow for single-molecule detection [11,12].

In conjunction with these adjectives, the development of nanomaterials has made a tremendous impact on a wide range of fields including catalysis, computing, photonics, energy, biology, and medicine, leading to an enormous interest in nanotechnology. Particularly, the utilization of nanotechnology in biological applications has shown a highly attractive potential [12]. In particular, silicon nanomaterials are ideal candidates for biosensors due to their low toxicity and favorable biocompatibility, both of which are crucial for biological and biomedical applications. Moreover, silicon nanomaterials offer tremendous surface-to-volume ratios allowing for outstanding optoelectronic properties, which have been extensively investigated for multiple applications, from solar cell technology to biology. These properties make it even more favorable for the design of nanosensors. In that regard, silicon nanoparticles (Si NPs) could offer solutions to some of the shortcomings that have arisen in biomedical applications, as silicon is known for its abundance, non-toxicity, and inertness [13]. Nonetheless, the application of NPs in a biological environment needs to be scrupulously studied from a fundamental standpoint. It has been consistently reported that when they are introduced *in vivo*, they get coated with protein aggregates called a protein corona, which will be in contact with biological tissues [14]. Thus the protein corona will have a deciding effect on the bio-applicability of NPs [14–16]. The NPs interactions with proteins have thus been thoroughly studied in the last decade to analyze which factors decide whether or not a protein molecule adsorbs at the particle surface [17–19]. The NP size has also been reported to be a significant factor in these interactions [20,21].

Thus, the interface between the nanostructure in the solid state and the biomolecule in solution requires significant attention as it dictates the biosensor performance and sensitivity. At this solid–liquid interface, the phenomenon of biomolecular adsorption on solid surfaces occurs. Protein adsorption on a solid surface could be either favored if the goal is cell attachment for example, or undesired in the case of biofouling [22,23]. Whenever a solid surface is placed in a solution containing a given protein, the protein will generally tend to rapidly adsorb until it saturates the surface. The final organization of the adsorbed protein layer (i.e., the orientation, conformation, and packing arrangement of the adsorbed proteins) depends on the chemical and physical structure of the protein, the surface, the aqueous solution, and the thermodynamics of the interactions between these system components [24,25]. This phenomenon includes a number of interactions at the solid–liquid interfaces that involve hydrophobic, electrostatic, and van der Waals interactions, as well as hydrogen bonding [26–29].

In the past few years, plenty of research has been focused on the understanding of the fundamental structure and physicochemical properties involved in the interactions between the proteins and the surfaces [30]. It is agreed upon that they are influenced by the protein's properties on one side and by the surface properties on the other. The factors that are most relevant include surface energy, polarity, charge, and morphology [31,32]. On the other hand, the properties of proteins that affect their interactions with surfaces are the size, charge, structure stability, and unfolding rate [33].

Since most substrates and proteins are charged, electrostatic interactions are crucially important. Therefore, electrostatic effects have received particular attention, especially since they can be controlled (using pH and ionic strength) and exploited to stabilize protein solutions against aggregation [34], or to reduce the rate of interfacial adsorption [35,36]. As non-covalent binding forces, electrostatic and/or hydrophobic interactions can be used as “physical” tools for the immobilization of proteins at

the surface of the sensing device. To this effect, hydrogenated nanocrystalline silicon (nc-Si:H) is an ideal candidate for biological applications, such as advanced biosensors, because of the local electric fields/dipoles present at its surface at the amorphous/crystalline contact zone, which can offer an effective control over the orientation of the immobilized proteins that is not easily achieved through non-covalent binding of biorecognition elements in biosensor devices [37], and which is crucial for the enhancement of biosensor sensitivity [38].

This work thus showcases the benefits of nc-Si:H NPs in the non-covalent binding and orientation of immobilized biomolecules. It will be divided in two parts: the first part is devoted to the preparation and analysis of nc-Si:H substrates. The adsorption of bovine serum albumin (BSA) proteins on these substrates will be discussed later. BSA is not used as a biorecognition element in biosensor devices but is commonly used as a model protein in molecular biology research and is thoroughly studied in literature. In the discussion section, a correlation between crystallinity, charge/polarity, morphology of the surfaces, and charge/structure of the protein molecules will be made with respect to the orientation of the adsorbed proteins on these heterogeneous surfaces.

## 2. Materials and Methods

Films of hydrogenated silicon were deposited via radiofrequency magnetron sputtering (RFMS) of a high purity crystalline silicon (99.9%) target, distanced from the substrate holder by 5 cm, under verified deposition conditions that produce nanocrystalline silicon. These parameters include a 2 Pa total pressure with 30%/70% partial pressures of Ar/H<sub>2</sub> (with a purity of 99.9999%). The RF power was set at 200W and the substrate temperature was fixed at 200 °C. Three corning glass substrates and one substrate of c-Si were used for each deposition session. These substrates were cleaned in ultrasonic baths of trichloroethylene, acetone, and distilled water, in that order, before they were introduced in the deposition chamber. This chamber was then pumped down to 10<sup>-7</sup> Torr before each run of the plasma.

In order to augment the density of nanocrystals, the films were treated immediately after deposition with 3Pa of molecular hydrogen at 200 °C for 20 min. The samples were analyzed with the purpose of showcasing their crystallinity in terms of crystallite density and size; Raman measurements were performed using a Jobin-Yvon T64000 Raman spectrometer (Horiba, Kyoto, Japan) at room temperature in the backscattering configuration. It is equipped with a monochromatic argon laser 514.5 nm, which was set at a low beam power (50 mW) to avoid any laser induced crystallization. X-ray diffraction (XRD) was carried out using an X-ray Bruker D8 Advance Diffractometer (Bruker, Billerica, MA, USA), with CuK<sub>α</sub> radiation ( $\lambda = 1.54 \text{ \AA}$ ). XRD patterns were taken at a grazing angle of 0.5° while varying the diffraction angle 2 $\theta$  from 20° to 60°. Atomic force microscopy (AFM) was performed in order to visualize the surface of the samples before protein adsorption, using a Dimension Edge Atomic Force Microscope (Bruker, Billerica, MA, USA) in the tapping mode at room temperature.

For the study of protein adsorption, these substrates were immersed in an aqueous solution of bovine serum albumin (BSA), which was prepared by diluting a measured amount of protein powder in a measured volume of Milli-Q water with the goal of obtaining a concentration of 1 g/L, and the pH was chosen at the starting value of 6.38. Protein adsorption on solid surfaces is known to be a quick process [39], which reaches saturation within one hour, followed by the process of desorption, which can last for several hours [40]. Thus, an incubation period of 24h was chosen, following BSA adsorption studies reported in References [39,40]. The samples were rinsed afterwards to eliminate non-attached proteins. The samples were then dried in air before analysis. The interactions of the proteins with the surfaces were analyzed using a Bruker FTIR spectrometer (ALPHA, Billerica, MA, USA) in the range of 400–4000 cm<sup>-1</sup>, with a resolution of 4 cm<sup>-1</sup>, in the attenuated total reflection (ATR) mode. AFM was also used to illustrate the effects caused by the protein adsorption on the surfaces of the films.

### 3. Results

#### 3.1. Surface Characterization

Raman spectroscopy is a powerful technique that is frequently used to characterize different silicon structures. It provides quantitative information about the crystallinity of the films. Figure 1 presents typical Raman spectra for the transverse optical (TO)-like mode, for the deposited and the treated samples. The deposited film clearly presents a mixed structure, evidenced by the broad shape of the band located around 450–550  $\text{cm}^{-1}$ , with an apparent shoulder around 510–520  $\text{cm}^{-1}$ , which is indicative of embedded crystallites in an amorphous network. This structure is called polymorphous silicon [41], hence we called this sample (PM). The after-deposition treatment clearly enhanced the crystallinity of the film, illustrated by the increase in both the intensity and the sharpness of the peak around 520  $\text{cm}^{-1}$ . Nonetheless, this sample still harbored an amorphous network, which is apparent due to the broad shape of the peak. We called this sample (NC) due to the overwhelming nanocrystallized network in the film.

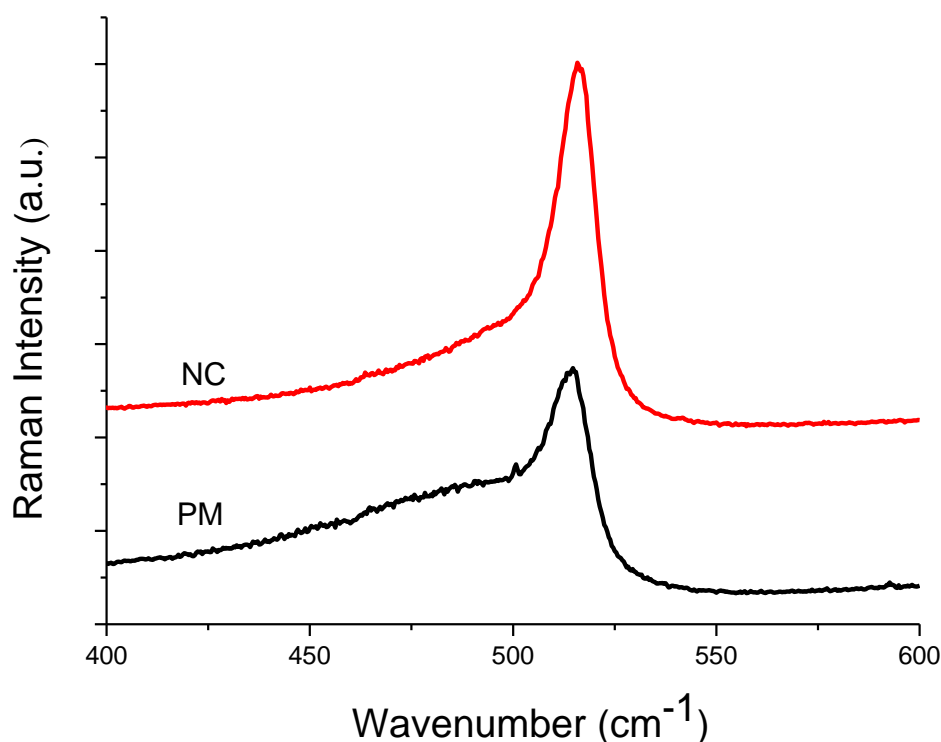


**Figure 1.** Raman scattering spectra illustrating the part related to the transverse optic (TO)-like mode of Si-Si vibrations for the deposited (PM) and treated (NC) films.

Figure S1 shows the deconvolution of the Raman spectrum, which was undergone in an effort to parse the complex structure of the material. The (TO)-like mode was fitted using three Gaussian bands corresponding to an amorphous phase presented by the usual broad band around 480  $\text{cm}^{-1}$ , an intermediate component around 510  $\text{cm}^{-1}$  that is indicative of the presence of small crystallites (<10 nm) [42], and a narrow band around 516  $\text{cm}^{-1}$  representing the crystalline tissue in the material. These sub-bands can be used to estimate the crystallite volume fraction of the material by calculating and summing the areas under the crystallite and intermediate components and then dividing by the sum of all the components:

$$X_c = \frac{I_c + I_i}{I_c + I_i + I_a} \quad (1)$$

Table 1 presents the results of the analysis of the TO-like mode, and shows that  $X_c$  was found to be 46% for the PM sample and 70 % for the NC sample.

**Table 1.** Structural analysis results of the Raman and XRD spectra. For Raman spectroscopy, it reports the positions and the integrated areas of each sub-band, as well as the crystalline volume fraction for each sample, and for XRD, it reports the position and the full width at half max of the (111) peak, as well the crystallite size.

Sample	Raman							XRD		
	Amorphous Phase		Intermediate Phase		Crystalline Phase			Position (°)	Diff. Peak (111)	
	Position (cm <sup>-1</sup> )	I <sub>480</sub> (%)	Position (cm <sup>-1</sup> )	I <sub>510</sub> (%)	Position (cm <sup>-1</sup> )	I <sub>520</sub> (%)	$X_c$ (%)		FWHM (°)	D (nm)
PM	487	54	509	24	515	22	46	28.2	0.82	10 ± 0.5
NC	481	30	508	36	516	34	70	28.4	0.72	11 ± 0.5

X-ray diffraction was used to shed light on the crystallographic orientations of the nanocrystals, and to measure their size. This measurement confirmed the enhancement of the crystallinity of the deposited film by the hydrogen treatment. Figure 2 shows diffraction peaks at 28°, 47°, and 56° corresponding to orientations (111), (220), and (311), respectively. These spectra have been normalized by subtracting a baseline; therefore, the increase in the intensity of the peaks was related to an increase in the crystallinity of the films. An XRD spectrum can be used to determine the average size of the crystallites in the films using the Scherrer formalism [43]. This can be achieved by determining the FWHM of the interference peaks ( $\Delta 2\theta$ ) at a given orientation using the Scherrer equation:

$$d = \frac{0.9\lambda}{\beta \cos \theta} \quad (2)$$

where  $d$  is the crystalline grain size,  $\lambda$  the wavelength of the x-rays,  $\beta$  is the full width at half maximum (FWHM) of a given peak, and  $\theta$  is the scattering angle.

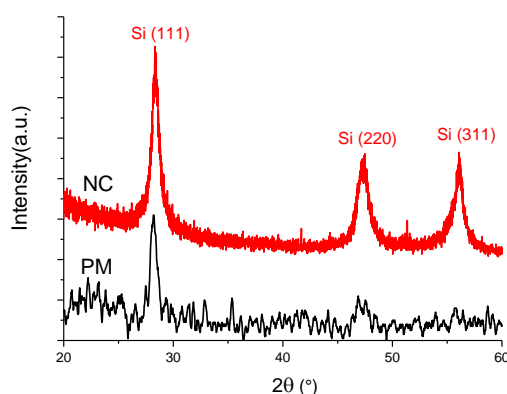


**Figure 2.** XRD patterns for the deposited (PM) and treated (NC) samples with different crystalline volume fractions.

The mean size of the crystallites was found to be 10–11 nm for the PM and NC films (see Table 1). Thus, the hydrogen treatment had an insignificant effect on the size of the crystallites. It can be then deduced that this treatment triggered the formation of nanocrystals within the amorphous structure [44].

An ellipsometric study of these samples revealed that the as-deposited (PM) film is a mixture of a crystalline phase contributing about 57% of the structure, an amorphous phase contributing about 29%, and the rest is void at around 14% showcasing the porosity of these films. On the other hand, the NC film was found to lodge an 18-nm thick subsurface layer consisting of about 71% crystallites, agreeing

with the Raman results, about 11% of a-Si:H, and up to 18% of void [44]. Thus, the NC surface was more homogenous than the PM surface.

Atomic force microscopy (AFM) was used to probe the morphological modifications of the surfaces as a result of the increased density of nanocrystals. 3D micrographs in the height mode of the PM and NC surfaces are shown in Figure 3. The surface of the PM film was smooth with sporadic clusters which were easily detectable by their enhanced contrast since they slightly stuck out of the plane. The smooth part that dominated the surface was in accordance with the amorphous nature of this sample [45,46], as revealed by Raman measurements. The clusters represented aggregated crystallites, which formed nc-Si:H NPs. The NC surface morphology appeared to be drastically different from the surface of the PM film, as the NPs became the dominant feature on the surface. Figure 3 also shows the cross section profiles of both samples; the PM sample's surface again appeared to be almost completely flat, characterized by a root mean square (RMS) roughness around 0.7 nm and a roughness average (Ra) around 0.5 nm, save a few spots that stuck out of the plane, which illustrate the NPs, as seen in the cross-section profile that shows a mountain that represents an NP. For the NC sample, the surface appeared to be less smooth, with a RMS roughness around 1.8 nm and an Ra around 1.4 nm, riddled with pointy grains, and an average height of  $\approx 8$  nm for the NPs, which was similar to the height of that peak in the PM profile.

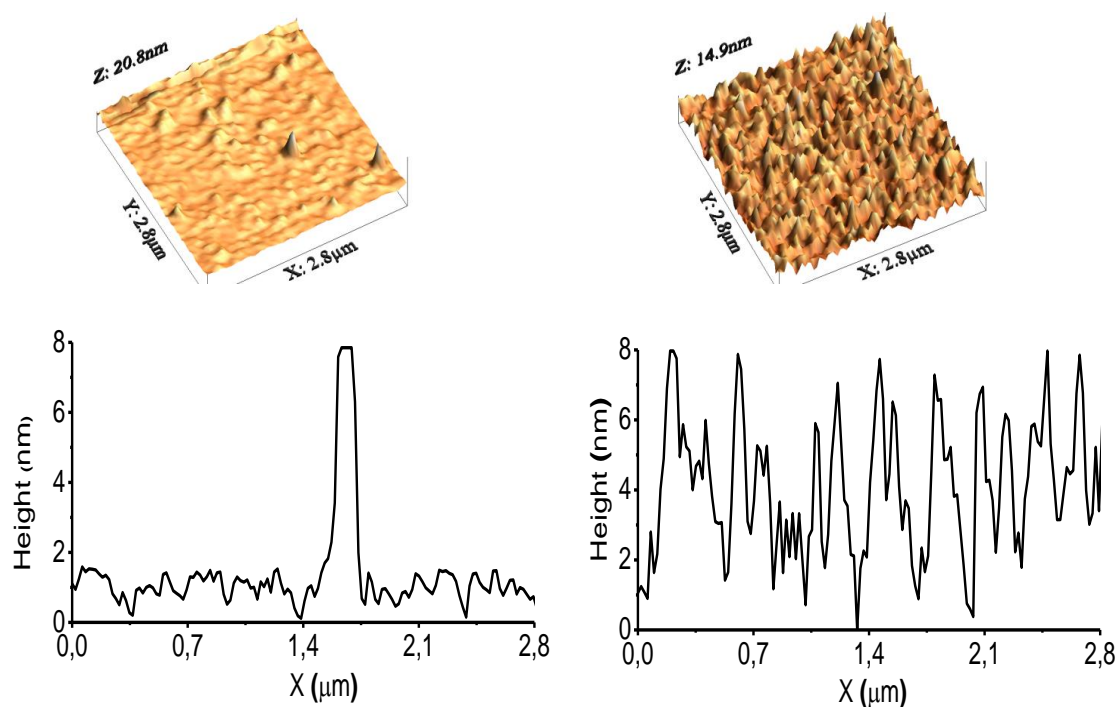


**Figure 3.** 3D topographical images (top) and 2D profiles (bottom) of surface areas in the height mode for the deposited (PM) surface (left) and the treated (NC) surface (right).

### 3.2. Protein–Surface Interaction Analysis

The analysis of the surfaces used in this study showed that they differed primarily in the density of nanocrystals, which were found to be around 45 and 70% for the PM and NC samples, respectively. The affinity of both substrates for proteins at the solid–liquid interface was studied using FTIR-ATR. Figure 4 shows the amide region in the IR spectra for the PM and NC samples after protein adsorption. It illustrates the amide I ( $1650\text{ cm}^{-1}$ ) and amide II ( $1550\text{ cm}^{-1}$ ) region. The amide I band was due mainly to the C=O stretching vibration and the amide II band was due to the N–H groups in the plane and the C–N stretching modes of polypeptide chains [47]. This region was used for both qualitative

and quantitative analysis, as the intensity of these bands is proportional to the amount of protein adsorbed on the surface [48].

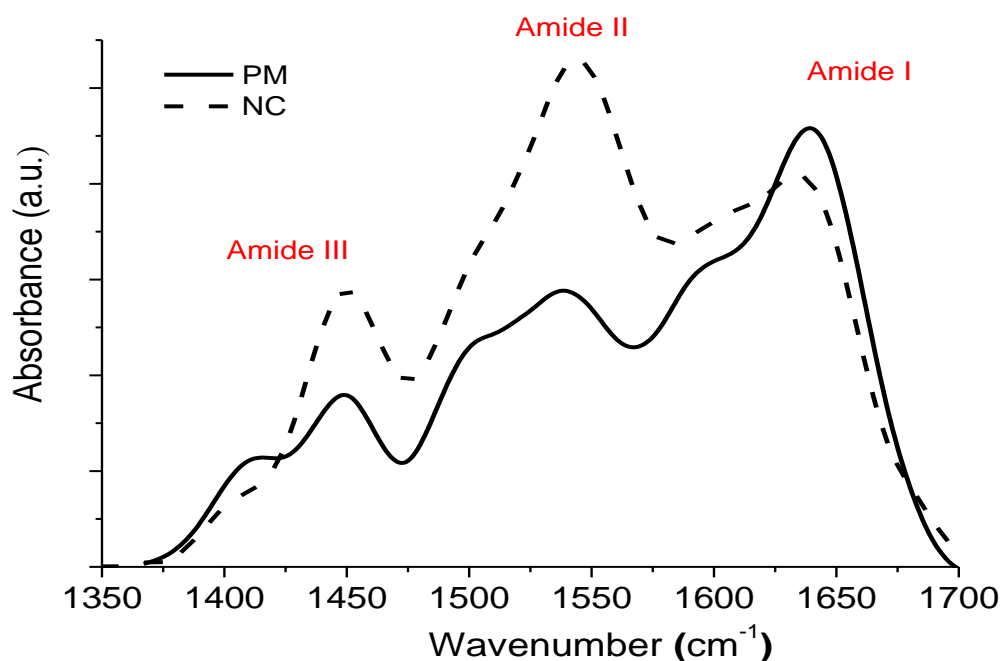


**Figure 4.** IR-ATR absorbance spectra of the amide region for adsorbed proteins on the deposited (PM) and treated (NC) substrates.

It is evident from the normalized absorbance spectra that the NC sample presents a much more intense amide II peak than the PM sample, which could be a sign of an enhanced adsorption on the NC substrate, as the amide II peak intensity was found to be 1.83 times higher than the peak intensity of the amide II band for the PM sample. The amide I and amide II bands were located at  $1639\text{ cm}^{-1}$  and  $1539\text{ cm}^{-1}$  for the proteins adsorbed on the PM substrate, and at  $1634\text{ cm}^{-1}$  and  $1544\text{ cm}^{-1}$  for the proteins adsorbed on the NC substrate. These position shifts indicate a different environment and/or a different structural arrangement of the proteins on the two surfaces.

The amide I and amide II band intensity ratio was also calculated, since it is thought to be indicative of orientation changes of protein molecules [48]. The amide I/II ratio was different for the two samples, as reported in Table 2. It was found to be 1.6 for the proteins adsorbed on the PM substrate, and 0.77 for the proteins adsorbed on the NC substrate. Combined with the knowledge of amide peak shifts, the amide I/II ratio implies that the BSA proteins orientation was different on the two surfaces. The amide I and II region can also be used to reveal informations about the secondary structure of the adsorbed proteins [49,50]. Therefore, the amide I bands were analyzed via curve fitting, the results of which are shown in Table 2. The bands centered around  $1650\text{--}1655\text{ cm}^{-1}$  have been assigned to  $\alpha$ -helices, the bands centered around  $1621\text{--}1640\text{ cm}^{-1}$  to  $\beta$ -sheets, and the bands centered around  $1663\text{--}1685\text{ cm}^{-1}$  to  $\beta$ -turns [48].

Table 2 reports the peak positions and proportions of the different components of the secondary structure of the adsorbed proteins for both samples. Figure S2 shows the curve fit of the amide I band of the PM and NC samples. The secondary structure of the proteins adsorbed on the PM substrate was composed of 18.4%  $\alpha$ -helix located at  $1655\text{ cm}^{-1}$  and two  $\beta$ -sheet components located at  $1625\text{ cm}^{-1}$  and  $1640\text{ cm}^{-1}$ , collectively making up 55.5% of the secondary structure. A band appeared around  $1605\text{ cm}^{-1}$  associated with inter-molecular  $\beta$ -sheets. Another peak appeared around  $1668\text{ cm}^{-1}$  associated with  $\beta$ -turns. The secondary structure of the proteins adsorbed on the NC substrate presented an overall similar structure; an  $\alpha$ -helix located at  $1654\text{ cm}^{-1}$  with a 19.8% proportion and

two  $\beta$ -sheets components located at  $1622\text{ cm}^{-1}$  and  $1639\text{ cm}^{-1}$ , collectively making up 50.4 % of the secondary structure. An inter-molecular  $\beta$ -sheet also appeared at  $1606\text{ cm}^{-1}$ . However, the  $\beta$ -turn peak was shifted to  $1679\text{ cm}^{-1}$ .

**Table 2.** Analysis of the secondary structure of adsorbed proteins.

Sample	Position	Area (%)	Assignment	Area $\beta/\alpha$	Max Amide I/II
PM	1605	20	Intermolecular $\beta$ sheet	3.01	1.6
	1625	20.5	$\beta$ sheet		
	1640	35	$\beta$ sheet		
	1655	18.4	$\alpha$ helix		
	1668	6.1	Turn		
NC	1606	22.8	Intermolecular $\beta$ sheet	2.55	0.77
	1622	23	$\beta$ sheet		
	1639	27.4	$\beta$ sheet		
	1654	19.8	$\alpha$ helix		
	1679	6.9	Turn		

The ratios of the areas under  $\beta$ -sheet to  $\alpha$ -helices ( $(I_{1640} + I_{1620})/I_{1655}$ ) provide a quantitative measure for the net change in the protein entropy. This ratio was  $<1$  for native BSA since its structure was dominated by  $\alpha$ -helices. It was found to be 3 for the proteins adsorbed on the PM substrate and 2.5 for the proteins adsorbed on the NC substrate. Thus, both surfaces induced the unfolding of the proteins as the  $\alpha$ -helix percentage drastically decreased for both samples. Therefore, the nanostructure at the surface did not appear to have had an effect on the adsorbed proteins conformation.

Atomic force microscopy was used to evaluate the coverage of the protein molecules and to analyze the morphology of the adsorbed protein layer. Figure 5 shows the 2D images of the PM and NC substrates before and after protein adsorption. For the PM sample, it is clear that the morphology of the adsorbed protein layer was not uniform. The image is dominated by a dark area (zone 1) that is contrasted by patches containing bright spots (zone 2). These two zones appear to be drastically different; zone 1 shows multiple black spots, while zone 2 shows a large bright spot with a high coverage area surrounding it. Cross-section profiles of a section that encompasses these two zones are also shown in Figure 5. These profiles reveal clearly that the black spots that appear in zone 1 of the 2D micrograph represent the bare a-Si:H part of the substrate, evidenced by the height in the profile that dips to below 2 nm, which is the same height in the profiles of the bare substrate shown in Figure 3. Between these uncovered spots, the profile rose by around 3–4 nm, which represents the height of the adsorbed proteins. The profile in zone 2 reveals the stiff elevation of two large bright spots that represent the crystallites on the surface. The height of the profile in this area rises up to around 13 nm which is much higher than the height of the crystallites shown in the profile (8 nm) in Figure 3. This illustrates that the proteins were adsorbed on top of the NPs. As the profile moves away from the peaks, it does not dip abruptly as in the profile shown in Figure 3, but it gradually decreases, which indicates that the proteins were coalesced around the crystallites, with a height around 8–9 nm. The reader should note the differences in the profile heights around and on top of the NPs, compared with the height on the amorphous part.

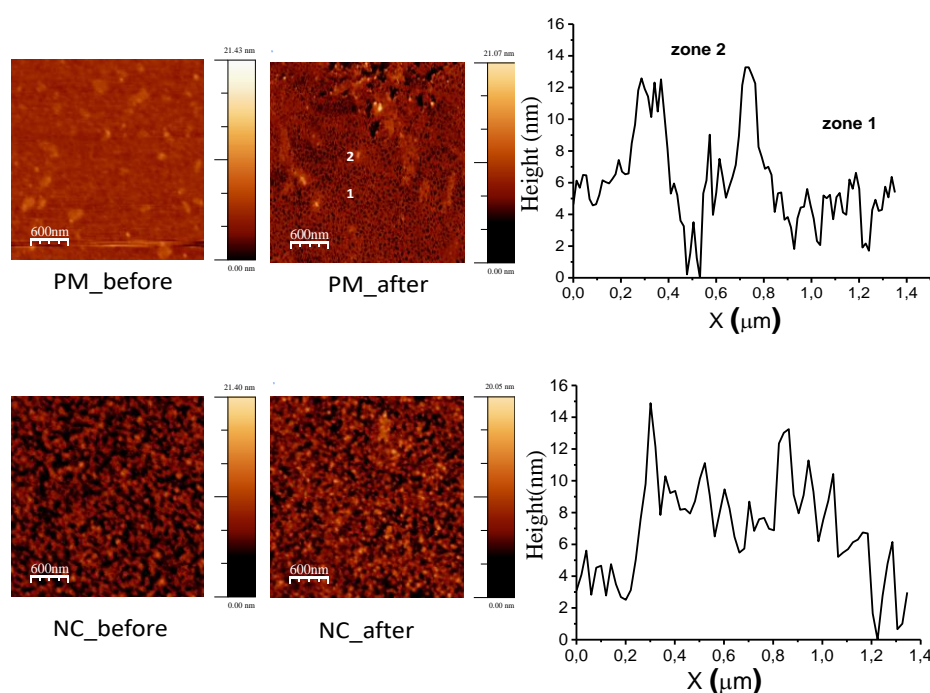


**Figure 5.** The topographical AFM 2D images before and after protein adsorption (left) and the cross section profiles after adsorption (right). Note the brightness difference on the spots when comparing the before and after adsorption images.

Figure 5 also shows the 2D image of the NC substrate before and after protein adsorption. Across the whole area, it shows a similar profile, which was not the case for the PM substrate. Every section of the micrograph after adsorption shows bright spots representing the NPs, wrapped by patches similar to zone 2 for the PM micrograph. It also shows dark spots representing the amorphous part of the substrate. The cross-section profile of a segment of the probed area shows that the peaks, which represent the crystallites on the surface, were as high as 13–15 nm, while the valleys between the peaks were as high as 8–9 nm, which illustrates the adsorbed proteins between and around the crystallites. As the profile moves to the dark areas, it dips sharply to around 4–5 nm indicating that this was the protein-covered amorphous region that was similar to zone 1 in the PM profile. These results illustrate that the morphology of the adsorbed film was different in the amorphous parts and crystalline parts, suggesting that there may be two distinct adsorption mechanisms occurring on these structurally different networks. These AFM observations require a quantitative study that involves the measurement of the adsorbed protein amount, following the methodology presented in [24], in order to provide a more complete assessment of the adsorption mechanism around the NPs on one hand, and on the a-Si:H part of the surface on the other hand. This would provide an estimate of the strength of the binding forces around the nanocrystals and correlate this with the qualitative results obtained using AFM that show that the adsorbed protein amount was significantly greater on the NC substrate compared with the PM substrate.

#### 4. Discussion

The contrast in the adsorption mechanisms can only be explained by the structure at the surface of the films. The PM surface was found to be dominated by an a-Si:H surface on which are embedded columnar NPs of nc-Si:H, the size of which were about 8 nm in height and 130 nm in diameter (Figure 3). The NC surface was, on the other hand, dominated by NPs. The structure at the NC surface was therefore much more homogenous than the PM surface. The IR spectral response of adsorbed proteins on this type of surface was the average response of molecules in interaction with

the a-Si:H surface and the proteins in interaction with the NPs. Therefore, we can suggest that the secondary structure modification was mostly driven by the silicon hydride network, which explains the overall similarity in the conformation of the adsorbed proteins on the two surfaces. A number of studies in the literature report that BSA proteins lose a significant part of their  $\alpha$ -helix structure when adsorbed on hydrogen-terminated surfaces [51,52]. In the case of hydrogenated silicon substrates, the non-polar SiH<sub>x</sub> at the surface interact with the protein molecules via hydrophobic forces that trigger their unfolding, and thus the loss of the  $\alpha$ -helix structure [53]. This unfolding allows the protein molecule to increase its contact zone with the surface, thereby maximizing the protein–surface interactions [54]. On the other hand, the contrast in the 2D AFM profile of the PM sample after protein adsorption can be explained by its heterogeneous structure, with a low protein coverage region over the a-Si:H area, and sporadic highly covered areas around the nc-Si:H NPs. For the NC sample, the similarity of the profile across the whole area was due to the high density of the NPs that interacted with the protein molecules that were adsorbed around the nanocrystals. This NP–protein interaction could be explained by the formation of a so-called corona (crown) around the NPs, which is a term used to explain the association of proteins with NPs in biological fluid [55]. Particles may bind different amounts and types of protein depending on the particle size, shape, and surface characteristics [56].

The binding forces that are asserted on the protein molecules can be analyzed via the full energy thermodynamic analysis of the interaction between proteins and the surface. It is described by the change of the Gibbs free energy ( $\Delta G$ ) of the system,  $\Delta G = \Delta H - T\Delta S$ , where  $T$  is the temperature and  $\Delta S$  and  $\Delta H$  are the entropy and enthalpy changes, respectively.  $\Delta G$  indicates whether a change of state is favorable. Protein adsorption is likely to occur only when the Gibbs energy  $G$  of the system, under constant temperature and pressure conditions, is lowered [57]. The changes in  $\Delta H$  and  $\Delta S$  help to identify the reaction dynamics between the surface and the proteins.  $\Delta H$  is the term that represents energy changes; if it is positive, the system benefits from a supply of energy from the external environment, which will lead to a change in the system. If it is negative, it indicates either a breaking or a formation of bonds, which releases energy.  $\Delta S$  on the other hand represents the changes in the molecular conformation of the proteins; if  $\Delta S > 0$ , the molecular structure of the proteins was spontaneously modified [58]. The likelihood of protein adsorption can be therefore enhanced by making either  $\Delta H$  highly negative or  $\Delta S$  highly positive, either through an external force acting on the proteins and/or via their unfolding through hydrophobic interactions [59].

A number of studies found in the literature show that NP–protein interactions follow negative enthalpy changes [60–62]. It has been concluded that when  $\Delta H < 0$ , the electrostatic forces drive the interactions because the other forces have lower energies [61,63], with one study reporting that they account for up to 80% of the total interactions of proteins with hydrogen-terminated nanocrystalline diamond films [61].

The electrostatic binding forces can explain the results of this study. These forces arise around the crystalline NPs at the junction between the amorphous and the crystalline regions, where we have two different semiconducting nanostructures with different band gaps; 1.2 eV for the crystalline region and  $\approx 1.9$  eV for the amorphous region. A space charge will therefore be formed due to the diffusion of free electrons from the more conductive crystalline region to the poorly conductive amorphous region (due to a much lower free electron density, see Figure 6) to establish thermodynamic equilibrium across the structure.

This space charge creates a local electric field (electrons and holes are oppositely charged) at the junction that can interact with charged and/or polar groups of the protein molecules. To calculate the strength of the electric field, we can model this space charge region (SCR) as a junction between an electron-rich region in the a-Si part of the junction and a hole-rich region in the c-Si part, therefore resembling a PN junction. However, it is necessary to assume that the electron and hole densities in the SCR are constant with respect to spatial coordinates, which is a gross oversimplification

since these charge carriers are assumed to be freely moving. Nevertheless, this will greatly simplify the derivation of the electric field  $E$  through the use of the Poisson equation:

$$\frac{dE}{dx} = \frac{\rho}{\epsilon_0 \epsilon_r} \quad (3)$$

where  $\rho$  is the charge density,  $\epsilon_0$  is the vacuum permittivity, and  $\epsilon_r$  is dielectric constant of silicon. Furthermore:

$$\begin{cases} \rho = -en, & x_a < x < 0 \\ \rho = ep, & 0 < x < x_c \end{cases} \quad (4)$$

where  $e$  is the electron charge,  $n$  and  $p$  are the equal electron and hole densities in c-Si at thermodynamic equilibrium, also known as intrinsic carrier densities  $n_i$  and  $p_i$ .

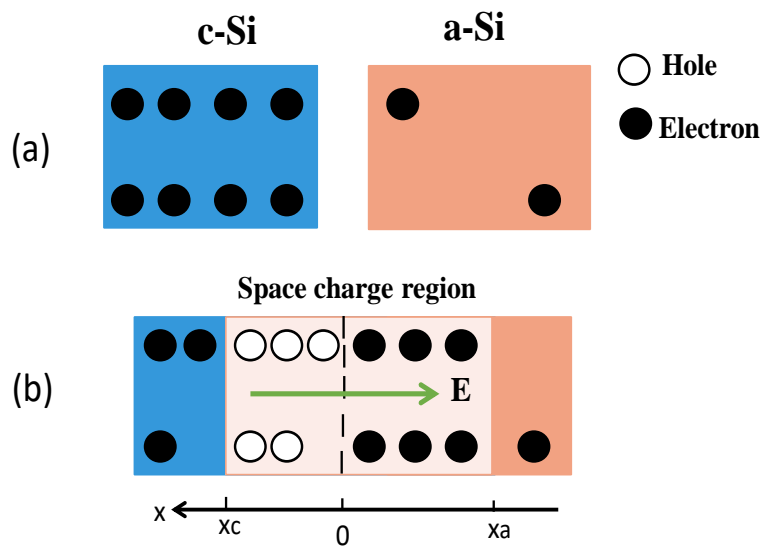


**Figure 6.** Schematic representation of the surface heterostructure showing the density of electrons on amorphous and crystalline silicon when separated (a) and in contact (b). Each structure is considered electrically neutral before contact. Note that electrons are negatively charged and holes are positively charged.

The resolution of these simple equations yields the electric field across the SCR:

$$\begin{cases} E(x) = \frac{-en_i}{\epsilon_0 \epsilon_r} (x - x_a), & x_a < x < 0 \\ E(x) = \frac{en_i}{\epsilon_0 \epsilon_r} (x - x_c), & 0 < x < x_c \end{cases} \quad (5)$$

The continuity of the electric field across the SCR implies that at the junction ( $x = 0$ ),  $E$  does not vary from the c-Si part to the a-Si part, which yields:

$$\|x_c\| = \|x_a\| = w, \quad (6)$$

where  $w$  is the width of the SCR in each part.

To calculate  $w$ , it is necessary to integrate Equation (3) to yield the electric potential  $V(x)$ , which necessitates the setting of boundary values for  $V(x = x_c) = V_c$  and  $V(x = x_a) = V_a$ . The potential difference ( $V_c - V_a$ ) is the built-in potential  $V_d$  across the junction which is a result of the potential barrier created by the diffusion of electrons at the contact between a-Si and c-Si. Setting the continuity condition for  $V(x)$  yields:

$$w^2 = \frac{\epsilon_0 \epsilon_r}{en_i} V_d \quad (7)$$

This in turn makes the electric field at the junction point of the SCR:

$$E(x = 0) = \sqrt{\frac{en_i}{\epsilon_0\epsilon_r}} V_d \quad (8)$$

$eV_d$  is the potential energy barrier, which is the difference in Fermi levels in a-Si and c-Si ( $\delta E_F$ ) while considering the conduction band levels for both structures, characterized by their electronic affinities, to be equal ( $\chi_{Si} = 4$  eV).

$E$  is thus estimated to be 25 V/cm for  $n_i$  around  $10^{10}$  cm<sup>-3</sup> for Si at room temperature and  $eV_d$  around 0.35 eV, considering the band gaps for both a-Si and c-Si, and that the Fermi levels in both cases to be in the middle of the gaps.

The strength of this electric field is 3 orders of magnitude lower than the transmembrane electric potentials, which are estimated to be in the range 10–250 mV across membranes with thicknesses in the range of 5–7 nm [64]. Therefore, the electric fields reported here do not mimic physiological conditions. It has been shown that upon the application of an external electric potential up to 200 V across a sample around 3  $\mu$ m thick, which would be around 4 orders of magnitude higher than the electric field in our study, no orientation changes were observed on the small peptide melittin [65]. Another study shows that the application of external fields of even higher magnitudes can dramatically disrupt the secondary structure of another small peptide (V3-loop), from a native  $\beta$ -sheet to  $\alpha$ -helix, through the rearrangement of amide dipole moments [66]. A recent simulation study shows that the application of strong external electric fields on the  $\alpha$ -helix dominant dihydrolipoamide dehydrogenase induces the despiralization of the helical structure to turns and random coils [67]. However, when it comes to much larger proteins, it has been shown that upon the application of external electric fields as low as 8 V/cm on the antibody immunoglobulin G (IgG), it is observed via AFM that the protein molecules are aligned in the direction of the applied field [68]. It should be noted that in that particular study, the electric field was laterally applied on the surface on which the proteins were physically adsorbed, mimicking the conditions of our study. The authors of that study noted that the use of lateral electric fields enables the biorecognition proteins to be oriented in a favorable direction, which enhances the sensitivity of the sensor device [68].

These electrostatic interactions lead to the reorientation of the protein molecules, which tend to expose their polar groups toward the surface in order to fully exploit the binding forces on the surface [69]. This exposure of like-charged molecules leads to inter-protein repulsive forces that makes aggregation around the nc-Si:H particles unlikely [32]. This seems to contradict the ATR-IR results that showed that the amide II peak for the NC sample in Figure 4 to be much more intense compared with the results of the PM sample. This could be explained by the fact that the amide I and amide II dipole moments were perpendicular to each other [49], which means that a particular orientation that aligns amide II dipoles of the adsorbed molecules around nc-Si:H NPs yields higher absorbance of the incident ATR beam. Therefore, the ATR data is better explained by a different alignment of amide II dipoles on the surface depending on the orientation of the adsorbed molecules than in terms of adsorption amount.

Thus, it is considered that the orientation of the adsorbed proteins around the crystalline NPs differed from those that were adsorbed on the amorphous part of the surface; to see where the protein molecules will tend to expose their hydrophobic parts to this hydrophobic surface, see Figure 7. The different orientations of the adsorbed proteins depending on the adsorption mechanism could explain the difference in the heights in the AFM profile in Figure 5, as the BSA molecule 3D shape was characterized by a heart-like shape with approximate dimensions of  $4 \times 4 \times 14$  nm<sup>3</sup> [70]. Although the unfolding of the molecules (as shown by the ATR-IR analysis) would drastically change this shape, the protein molecules would still be adsorbed along either its short axis (end-on adsorption) or its long axis (side-on adsorption), which explains the difference in the heights of the adsorbed protein layer. The unfolding of the protein molecules near the surface appears to be independent of the adsorption

mechanism, that is hydrophobic on the a-Si:H part of the surface and electrostatic around nc-Si:H particles. Thus, the reorientation of the molecules does not seem to reverse their denaturation.

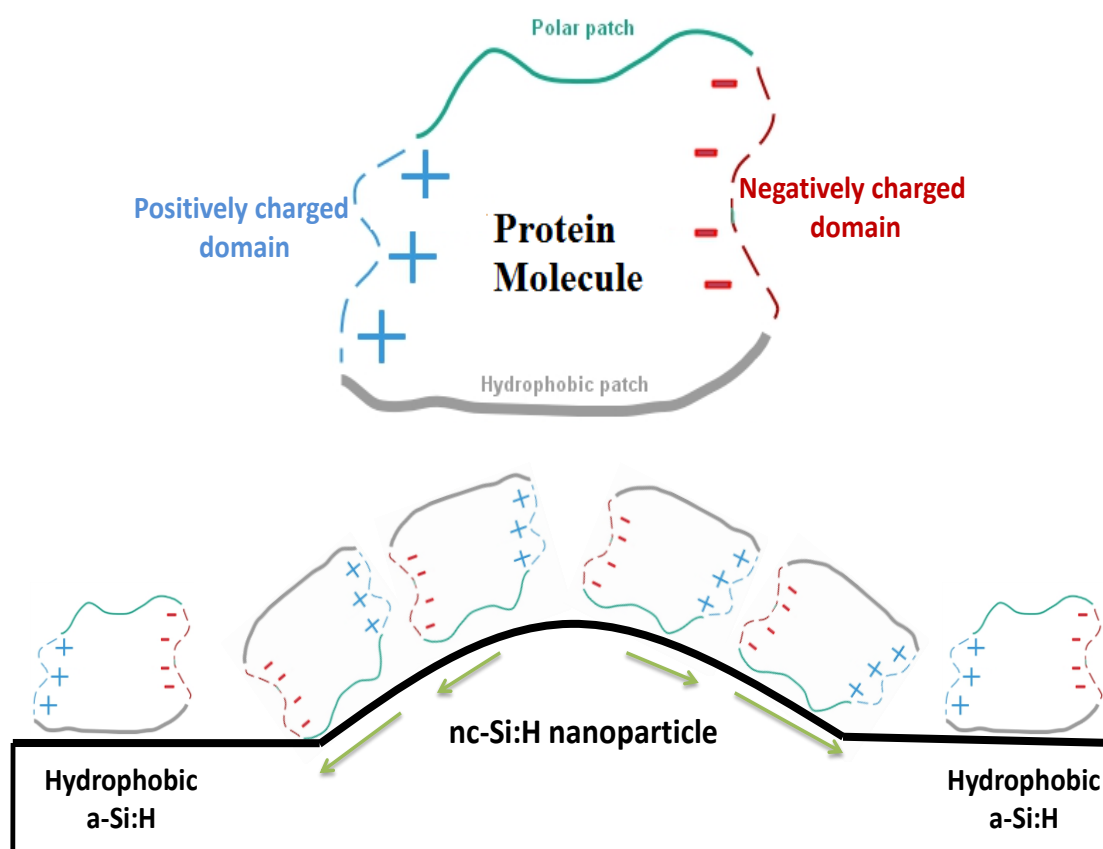


**Figure 7.** Schematic illustration of protein–surface interactions with different adsorption mechanism possibilities depending on the physicochemical characteristics of both the surface and the proteins. The green arrows on the nc-Si:H NPs symbolize electric fields.

## 5. Conclusions

The surface nanostructure effect on the binding mechanisms of bovine serum albumin molecules was studied, because of its vital importance for biosensor platforms, using substrates with a varying density of hydrogenated nanocrystalline silicon nanoparticles embedded in an amorphous network. The findings show that when the proteins were in contact with hydrogenated amorphous silicon, they adsorbed mainly via hydrophobic interactions with the surface. However, when they encountered nanoparticles, they interacted via electrostatic forces that arose at the junction between the amorphous and the crystalline parts of the structure, creating electric fields that were potent enough to trigger the reorientation of the molecules. The adsorbed proteins were found to be denatured regardless of the binding mechanism, which means that this electric field driven reorientation did not reverse the unfolding of the proteins. These results can open the door for non-covalent binding of antibodies serving as recognition elements in biosensors, with an additional and significant tool that is the control of their orientation vis-à-vis the surface to maximize the sensitivity of the device. Future work will be dedicated to the preparation of surface nanostructures tailored specifically to manipulate the orientation of surface-bound biomolecules.

**Supplementary Materials:** The following are available online at <http://www.mdpi.com/2571-9637/2/2/30/s1>. Figure S1. Decomposition of the TO-mode for the NC sample, and Figure S2. Curve fitting of the amide I bands from Figure 4.

**Author Contributions:** Conceptualization, L.F., Y.B. (Yamina Brahmi), J.D.S., and A.B.; methodology, L.F., Y.B. (Yamina Brahmi), A.B., Y.B. (Yahya Bouizem), A.K., D.B., and L.C.; software, Y.B. (Yahya Bouizem); formal analysis, L.F., Y.B. (Yamina Brahmi), J.D.S., and F.K.; investigation, L.F., Y.B. (Yamina Brahmi), K.Z., and N.L.; resources, J.D.S., D.B., K.Z., A.K., and L.C.; writing—original draft preparation, L.F. and Y.B. (Yamina Brahmi); writing—review and editing, L.F., J.D.S., and F.K.; supervision, J.D.S.; funding acquisition, J.D.S., A.K., and L.C.

**Funding:** This research received no external funding.

**Acknowledgments:** The authors would like to thank Pr. M. Ghamnia from the Laboratoire des Sciences de la Matière Condensée, Université Oran 1 Ahmed Ben Bella, Algeria, for the assistance in the AFM experiments.

**Conflicts of Interest:** The authors declare no conflict of interest.

## References

1. Pilehvar, S.; Wael, K.D. Recent Advances in Electrochemical Biosensors Based on Fullerene-C60 Nano-Structured Platforms. *Biosensors* **2015**, *5*, 712–735. [[CrossRef](#)] [[PubMed](#)]
2. Bhalla, N.; Jolly, P.; Formisano, N.; Estrela, P. Introduction to Biosensors. *Essays Biochem.* **2016**, *60*, 1–8. [[CrossRef](#)] [[PubMed](#)]
3. Eggins, B.R. *Chemical Sensors and Biosensors*; Wiley & Sons: Chichester, UK, 2002; Chapter 1; pp. 2–5.
4. Wilson, J.S. *Sensor Technology Handbook*; Elsevier: Oxford, UK, 2004; Chapter 6; p. 161.
5. Chandran, K.; Rajkumar, R.; Bhagrava, K. *Biosensors and Bioelectronics*; Elsevier: Amsterdam, The Netherlands, 2015; Chapter 1; pp. 2–66.
6. Touhami, A. *Nanomedicine*; One Central Press: Cheshire, UK, 2014; Chapter 15; p. 377.
7. Zhang, X.; Ju, H.; Wang, J. *Electrochemical Sensors, Biosensors and their Biomedical Applications*; Academic Press: San Diego, CA, USA, 2008; Chapter 3; p. 58.
8. Ding, J.; Qin, W. Potentiometric sensing of nuclease activities and oxidative damage of single-stranded DNA using a polycation-sensitive membrane electrode. *Biosens. Bioelectr.* **2013**, *47*, 559–565. [[CrossRef](#)] [[PubMed](#)]
9. Arora, P.; Sindhu, A.; Dilbaghi, N.; Chaudhury, A. Biosensors as innovative tools for the detection of food borne pathogens. *Biosens. Bioelectr.* **2011**, *28*, 1–12. [[CrossRef](#)]
10. Qi, M.; Zhao, K.; Bao, Q.; Pan, P.; Zhao, Y.; Yang, Z.; Wang, H.; Wei, J. Adsorption and Electrochemical Detection of Bovine Serum Albumin Imprinted Calcium Alginate Hydrogel Membrane. *Polymers* **2019**, *11*, 622. [[CrossRef](#)]
11. Adams, K.L.; Puchades, M.; Ewing, A.G. In Vitro Electrochemistry of Biological Systems. *Anal. Rev. Anal. Chem. (Palo Alto Calif.)* **2008**, *1*, 329–355. [[CrossRef](#)]
12. Peng, F.; Su, Y.; Zhong, Y.; Fan, C.; Lee, S.-T.; He, Y. Silicon Nanomaterials Platform for Bioimaging, Biosensing, and Cancer Therapy. *Acc. Chem. Res.* **2014**, *47*, 612–623. [[CrossRef](#)]
13. Pavesi, L.; Turan, R. *Silicon Nanocrystals*; Wiley-VCH Verlag: Weinheim, Germany, 2010; Chapter 1; pp. 1–4.
14. Monopoli, M.P.; Aberg, C.; Salvati, A.; Dawson, K.A. Biomolecular coronas provide the biological identity of nanosized materials. *Nat. Nanotechnol.* **2012**, *7*, 779. [[CrossRef](#)]
15. Saptarshi, S.R.; Duschl, A.; Lopata, A.L. Interaction of nanoparticles with proteins: Relation to bio-reactivity of the nanoparticle. *J. Nanobiotechnol.* **2013**, *11*, 26. [[CrossRef](#)]
16. Givens, B.E.; Diklich, N.D.; Fiegel, J.; Grassian, V.H. Adsorption of bovine serum albumin on silicon dioxide nanoparticles: Impact of pH on nanoparticle–protein interactions. *Biointerphases* **2017**, *12*, 02D404. [[CrossRef](#)]
17. Nel, A.E.; Mädler, L.; Velegol, D.; Xia, T.; Hoek, E.M.V.; Somasundaran, P.; Klaessig, F.; Castranova, V.; Thompson, M. Understanding biophysicochemical interactions at the nano-bio interface. *Nat. Mater.* **2009**, *8*, 543–557. [[CrossRef](#)]
18. Shemetov, A.A.; Nabiev, I.; Sukhanova, A. Molecular interaction of proteins and peptides with nanoparticles. *ACS Nano* **2012**, *6*, 4585–4602. [[CrossRef](#)]
19. Meissner, J.; Prause, A.; Bharti, B.; Findenegg, G.H. Characterization of protein adsorption onto silica nanoparticles: Influence of pH and ionic strength. *Colloid Polym. Sci.* **2015**, *293*, 3381–3391. [[CrossRef](#)]
20. Kurylowicz, M.; Giuliani, M.; Dutcher, J.R. Using nanoscale substrate curvature to control the dimerization of a surface-bound protein. *ACS Nano* **2012**, *6*, 10571–10580. [[CrossRef](#)]
21. Shang, W.; Nuffer, J.H.; Muniz-Papandrea, V.A.; Colón, W.; Siegel, R.W.; Dordick, J.S. Cytochrome C on silica nanoparticles: Influence of nanoparticle size on protein structure, stability, and activity. *Small* **2009**, *5*, 470–476. [[CrossRef](#)]

22. Valencia-Serna, J.; Chevallier, P.; Bahadur, K.C.R.; Laroche, G.; Uludag, H. Fibronectin-modified surfaces for evaluating the influence of cell adhesion on sensitivity of leukemic cells to siRNA nanoparticles. *Nanomedicine* **2016**, *11*, 1123–1138. [[CrossRef](#)]
23. Scarangella, A.; Soumbo, M.; Villeneuve-Faure, C.; Mlayah, A.; Bonafos, C.; Monje, M.-C.; Roques, C.; Makasheva, K. Adsorption properties of BSA and DsRed proteins deposited on thin SiO<sub>2</sub> layers: Optically non-absorbing versus absorbing proteins. *Nanotechnology* **2018**, *29*, 115101. [[CrossRef](#)]
24. Hasan, V.; Saxena, L.; Pandey, M. Surface Functionalization of Ti6Al4V via Self-assembled Monolayers for Improved Protein Adsorption and Fibroblast Adhesion. *Langmuir* **2018**, *34*, 3494–3506. [[CrossRef](#)]
25. Hasan, G.; Waibhaw, L.; Pandey, M. Conformational and Organizational Insights into Serum Proteins during Competitive Adsorption on Self-Assembled Monolayers. *Langmuir* **2018**, *34*, 8178–8194. [[CrossRef](#)]
26. Richter, A.G.; Kuzmenko, I. Using in Situ X-ray Reflectivity to Study Protein Adsorption on Hydrophilic and Hydrophobic Surfaces: Benefits and Limitations. *Langmuir* **2013**, *29*, 5167–5180. [[CrossRef](#)]
27. Silin, V.; Weetall, H.; Vanderah, D.J. SPR Studies of the Nonspecific Adsorption Kinetics of Human IgG and BSA on Gold Surfaces Modified by Self-Assembled Monolayers (SAMs). *Colloid Interface Sci.* **1997**, *185*, 94–103. [[CrossRef](#)]
28. Guo, S.; Pranantyo, D.; Kang, E.-T.; Loh, X.J.; Zhu, X.; Jańczewski, D.; Neoh, K.G. Dominant Albumin–Surface Interactions under Independent Control of Surface Charge and Wettability. *Langmuir* **2018**, *34*, 1953–1966. [[CrossRef](#)]
29. Azioune, M.; Chehimi, M.; Miksa, B.; Basinska, T.; Slomkowski, S. Hydrophobic protein– polypyrrole interactions: The role of van der Waals and Lewis acid– base forces as determined by contact angle measurements. *Langmuir* **2002**, *18*, 1150–1156. [[CrossRef](#)]
30. Mielczarski, J.A.; Dong, J.; Mielczarski, E. Real time evaluation of composition and structure of concanavalin A adsorbed on a polystyrene surface. *J. Phys. Chem. B* **2008**, *112*, 5228–5237. [[CrossRef](#)]
31. Hlady, V.; Buijs, J.; Jennissen, H.P. *Amyloid, Prions, and Other Protein Aggregates*; Elsevier: San Diego, CA, USA, 1999; Volume 39, p. 402.
32. Rabe, M.; Verdes, D.; Seeger, S. Understanding protein adsorption phenomena at solid surfaces. *Adv. Colloid Interface Sci.* **2011**, *162*, 87–106. [[CrossRef](#)]
33. Dee, K.C.; Puleo, D.A.; Bizios, R. *An Introduction to Tissue-Biomaterial Interactions*; Wiley-Liss: Hoboken, NJ, USA, 2002; Chapter 3; pp. 37–41.
34. Roberts, J. Non-native protein aggregation kinetics. *Biotechnol. Bioeng.* **2007**, *98*, 927–938. [[CrossRef](#)]
35. Nelson, N.; Schwartz, D.K. Specific Ion (Hofmeister) Effects on Adsorption, Desorption, and Diffusion at the Solid–Aqueous Interface. *J. Phys. Chem. Lett.* **2013**, *4*, 4064–4068. [[CrossRef](#)]
36. McUmbur, A.C.; Randolph, T.W.; Schwartz, D.K. Electrostatic Interactions Influence Protein Adsorption (but Not Desorption) at the Silica-Aqueous Interface. *J. Phys. Chem. Lett.* **2015**, *6*, 2583–2587. [[CrossRef](#)]
37. Trilling, K.; Beekwilder, J.; Zuilhof, H. Antibody orientation on biosensor surfaces: A minireview. *Analyst* **2013**, *138*, 1619. [[CrossRef](#)]
38. Tajima, N.; Takai, M.; Ishihara, K. Significance of antibody orientation unraveled: Well-oriented antibodies recorded high binding affinity. *Anal. Chem.* **2011**, *83*, 1969–1976. [[CrossRef](#)]
39. Mavropoulos, E.; Costa, A.M.; Costa, L.T.; Achete, C.A.; Mello, A.; Granjeiro, J.M.; Rossi, A.M. Adsorption and bioactivity studies of albumin onto hydroxyapatite surface. *Colloids Surf. B Biointerfaces* **2011**, *83*, 1–9. [[CrossRef](#)]
40. Stan, M.S.; Cinteza, L.O.; Petrescu, L.; Mernea, M.A.; Calborean, O.; Mihailescu, D.F.; Sima, C.; Dinischiotu, A. Dynamic analysis of the interactions between Si/SiO<sub>2</sub> quantum dots and biomolecules for improving applications based on nano-bio interfaces. *Sci. Rep.* **2018**, *8*, 5259. [[CrossRef](#)]
41. RocaiCabarcas, P. Plasma enhanced chemical vapor deposition of amorphous, polymorphous and microcrystalline silicon films. *J. Non-Crys. Solids* **2000**, *266–269*, 31–37. [[CrossRef](#)]
42. Amrani, R.; Abboud, P.; Chahed, L.; Cuminal, Y. Low Temperature Growth of Hydrogenated Silicon Prepared by PECVD from Argon Diluted Silane Plasma. *Cryst. Struct. Theory Appl.* **2012**, *1*, 62–67. [[CrossRef](#)]
43. Scherrer, P. Nachrichten von der Gesellschaft der Wissenschaften zu Göttingen. *Mathematisch-Physikalische Klasse* **1918**, *26*, 98–100.
44. Filali, L.; Brahmi, Y.; Sib, J.D.; Kail, F.; Bouizem, Y.; Benlakehal, D.; Zellama, K.; Bouhekka, A.; Kebab, A.; Chahed, L. Molecular hydrogen-induced nucleation of hydrogenated silicon nanocrystals at low temperature. *Surf. Interface Anal.* **2019**, *51*, 531–540. [[CrossRef](#)]

45. Boldyryeva, H.; Honda, S.; Mackova, A.; Mates, T.; Fejfar, A.; Kocka, J. Characterization of hydrogen contained in passivated poly-Si and microcrystalline-Si by ERDA technique. *Surf. Interface Anal.* **2006**, *38*, 819–822. [[CrossRef](#)]
46. Álvarez-Macías, C.; Monroy, B.M.; Huerta, L.; Canseco-Martínez, M.A.; Picquart, M.; Santoyo-Salazar, J.; García Sánchez, M.F.; Santana, G. Chemical and structural properties of polymorphous silicon thin films grown from dichlorosilane. *Appl. Surf. Sci.* **2013**, *285*, 431–439. [[CrossRef](#)]
47. Belfer, S.; Fainctain, R.; Purinson, Y.; Kedem, O. Surface characterization by FTIR-ATR spectroscopy of polyethersulphone membranes-unmodified, modified and protein fouled. *Membr. Sci.* **2000**, *172*, 113–124. [[CrossRef](#)]
48. Lenk, T.J.; Horbett, T.A.; Ratner, B.D.; Chittur, K.K. Infrared spectroscopic studies of time-dependent changes in fibrinogen adsorbed to polyurethanes. *Langmuir* **1991**, *7*, 1755. [[CrossRef](#)]
49. Roach, P.; Farrar, D.; Perry, C.C. Interpretation of Protein Adsorption: Surface-Induced Conformational Changes. *J. Am. Chem. Soc.* **2005**, *127*, 8168–8173. [[CrossRef](#)]
50. Chittur, K.K. FTIR/ATR for protein adsorption to biomaterial surfaces. *Biomaterials* **1998**, *19*, 357–369. [[CrossRef](#)]
51. Lubambo, A.F.; Benelli, E.M.; Klein, J.J.; Schreiner, W.H.; Silveira, E.; de Camargo, P.C. Tuning protein GlnB-Hs surface interaction with silicon: FTIR-ATR, AFM and XPS study. *Colloids Surf. B Biointerfaces* **2013**, *102*, 348–353. [[CrossRef](#)]
52. Awsiuk, K.; Budkowski, A.; Marzec, M.M.; Petrou, P.; Rysz, J.; Bernasik, A. Effects of polythiophene surface structure on adsorption and conformation of bovine serum albumin: A multivariate and multitechnique study. *Langmuir* **2014**, *30*, 13925. [[CrossRef](#)]
53. Filali, L.; Brahmi, Y.; Sib, J.D.; Bouhekka, A.; Benlakehal, D.; Bouizem, Y.; Kebab, A.; Chahed, L. The effect of amorphous silicon surface hydrogenation on morphology, wettability and its implication on the adsorption of proteins. *Appl. Surf. Sci.* **2016**, *384*, 107–115. [[CrossRef](#)]
54. Brahmi, Y.; Filali, L.; Sib, J.D.; Bouhekka, A.; Benlakehal, D.; Bouizem, Y.; Kebab, A.; Chahed, L. Conformational study of protein interactions with hydrogen-passivated amorphous silicon surfaces: Effect of pH. *Appl. Surf. Sci.* **2017**, *424*, 394–402. [[CrossRef](#)]
55. Cedervall, T.; Lynch, I.; Lindman, S.; Berggård, T.; Thulin, E.; Nilsson, H.; Dawson, K.A.; Linse, S. Understanding the nanoparticle-protein corona using methods to quantify exchange rates and affinities of proteins for nanoparticles. *Proc. Natl. Acad. Sci. USA* **2007**, *104*, 2050–2055. [[CrossRef](#)]
56. Cedervall, T.; Lynch, I.; Foy, M.; Berggård, T.; Donnelly, S.C.; Cagney, G.; Linse, S.; Dawson, K.A. Detailed Identification of Plasma Proteins Adsorbed on Copolymer Nanoparticles. *Angew. Chem.* **2007**, *119*, 5856–5858. [[CrossRef](#)]
57. Norde, W. Driving forces for protein adsorption at solid surfaces. *Macromol. Symp.* **1996**, *103*, 5–18. [[CrossRef](#)]
58. Sun, S.F. *Physical Chemistry of Macromolecules*; John Wiley & Sons, Inc.: Hoboken, NJ, USA, 2004; Chapter 4; p. 77.
59. Frauenfelder, H. *The Physics of Proteins*; Springer: New York, NY, USA, 2010; Chapter 18; p. 253.
60. Podila, R.; Chen, R.; Ke, P.C.; Brown, J.M.; Rao, M. Effects of surface functional groups on the formation of nanoparticle-protein corona. *Appl. Phys. Lett.* **2012**, *101*, 263701. [[CrossRef](#)]
61. Kloss, F.R.; Gassner, R.; Preiner, J.; Ebner, A.; Larsson, K.; Hächl, O.; Tuli, T.; Rasse, M.; Moser, D.; Laimer, K.; et al. The role of oxygen termination of nanocrystalline diamond on immobilisation of BMP-2 and subsequent bone formation. *Biomaterials* **2008**, *29*, 2433–2442. [[CrossRef](#)]
62. Maleki, M.S.; Moradi, O.; Tahmasebi, S. Adsorption of albumin by gold nanoparticles: Equilibrium and thermodynamics studies. *Arab. J. Chem.* **2017**, *10*, s491–s502. [[CrossRef](#)]
63. Aramesh, M.; Shimoni, O.; Ostrikov, K.; Praver, S.; Cervenka, J. Surface charge effects in protein adsorption on nanodiamonds. *Nanoscale* **2015**, *7*, 5726. [[CrossRef](#)] [[PubMed](#)]
64. Tsong, T.Y.; Astumian, R.D. Electroconformational Coupling: How Membrane-Bound ATPase Transduces Energy from Dynamic Electric Fields. *Annu. Rev. Physiol.* **1988**, *50*, 273–290. [[CrossRef](#)] [[PubMed](#)]
65. Le Saux, A.; Ruyschaert, J.; Goormaghtigh, E. Membrane molecule reorientation in an electric field recorded by attenuated total reflection Fourier-transform infrared spectroscopy. *Biophys. J.* **2001**, *80*, 324–330. [[CrossRef](#)]
66. Ojeda-May, P.; Garcia, M.E. Electric Field-Driven Disruption of a Native  $\beta$ -Sheet Protein Conformation and Generation of a Helix-Structure. *Biophys. J.* **2010**, *99*, 595–599. [[CrossRef](#)]

67. Jiang, Z.; You, L.; Dou, W.; Sun, T.; Xu, P. Effects of an Electric Field on the Conformational Transition of the Protein: A Molecular Dynamics Simulation Study. *Polymers* **2019**, *11*, 282. [[CrossRef](#)]
68. Emaminejad, S.; Javanmard, M.; Gupta, C.; Chang, S.; Davis, R.W.; Howe, R.T. Tunable control of antibody immobilization using electric field. *Proc. Natl. Acad. Sci. USA* **2015**, *117*, 1995–1999. [[CrossRef](#)]
69. Poncin-Epaillard, F.; Vrlinic, T.; Debarnot, D.; Mozetic, M.; Coudreuse, A.; Legeay, G.; El Moualij, B.; Zorzi, W. Surface Treatment of Polymeric Materials Controlling the Adhesion of Biomolecules. *J. Funct. Biomater.* **2012**, *3*, 528–543. [[CrossRef](#)]
70. McClellan, S.J.; Franses, E.I. Adsorption of bovine serum albumin at solid/aqueous interfaces. *Colloid Surf. A Physicochem. Eng. Asp.* **2005**, *260*, 265–275. [[CrossRef](#)]



© 2019 by the authors. Licensee MDPI, Basel, Switzerland. This article is an open access article distributed under the terms and conditions of the Creative Commons Attribution (CC BY) license (<http://creativecommons.org/licenses/by/4.0/>).